ChemComm
Chemical Communications

Accepted Manuscript

This article can be cited before page numbers have been issued, to do this please use: S. Chen, M. Liu, Z. Yang, Y. Zhang, J. Liu, W. Wu, T. Huang and H. Liu, *Chem. Commun.*, 2025, DOI: 10.1039/D5CC02859K.




ROYAL SOCIETY OF CHEMISTRY

rsc.li/chemcomm

View Article Online
DOI: 10.1039/D5CC02859K

COMMUNICATION

# Boosting Lithium-Ion Transport in Halide Solid-State Electrolytes by Aliovalent Substitution for All-Solid-State Lithium-Ion Batteries

Received 00th January 20xx,
Accepted 00th January 20xx

DOI: 10.1039/x0xx00000x

Suyue Chen,[a,†] Meiling Liu,[a,†] Zhihao Yang,[a] Yaxue Zhang,[a] Jiaxing Liu,[a] Weiying Wu,[a] Tieqi Huang, *[a,b] and Hongtao Liu,*[a,b]

**We report a novel chemical aliovalent substitution strategy that induces lithium vacancy generation, expands 3D $Li^+$ migration channels, and reduces activation energy. The optimized composition $Li_{1.8}Zr_{0.8}Nb_{0.2}Cl_6$ achieves a room-temperature ionic conductivity twice higher than that of pristine $Li_2ZrCl_6$, realizing stable cycling in all-solid-state lithium-ion batteries.**

Among emerging battery technologies, all-solid-state lithium-ion batteries (ASSLIBs) stand out as promising candidates due to their superior thermal stability, safety, and energy density compared to conventional lithium-ion batteries (LIBs).[1,2] By replacing flammable organic liquid electrolytes with solid-state electrolytes (SSEs), ASSLIBs eliminate combustion risks, significantly enhancing safety for both vehicles and passengers. Additionally, the integration of SSEs with lithium metal anodes offers a competitive edge in energy density and safety over traditional LIBs[3,4].

Inorganic halide SSEs emerge as a promising alternative, offering high ionic conductivity (typically in the range of $10^{-4}$~$10^{-3}$ S $cm^{-1}$) [5], excellent mechanical ductility, and superior oxidation resistance, which make it particularly compatible with high-voltage cathode materials. Since the breakthrough discovery by Asano et al.[6] in 2018 of trigona $Li_3YCl_6$ and monoclinic $Li_3YBr_6$ with excellent ionic conductivity at room temperature, halide SSEs have garnered significant attention. Subsequent studies on $Li_3MCl_6$-like materials (where M = Sc, In, Er, Y, etc.) have further validated their potential.[7] Compared to chlorides using transition metals such as $Li_3YCl_6$ and $Li_3InCl_6$, $Li_2ZrCl_6$ with high abundance of $ZrCl_4$ as the raw material has a significant cost edge. Moreover, no additional sintering is required and its own synthesis step is simple. The low-cost and convenient synthesis method promotes its commercialization possibility. However, its ionic conductivity at room temperature is poor (~ 0.4 × $10^{-3}$ S $cm^{-1}$), and how to further improve the ionic conductivity is still the core direction of current research.

Aliovalent substitution has proven effective in tailoring vacancy-mediated ion transport.[8–11] However, excessive substitution risks doping failures or phase transitions, underscoring the need for precise dopant selection.[12] High-valent and small-radius metal elements can introduce vacancies to reduce the average potential of $Li^+$ and improve the cation potential, which promotes ion migration.[13,14] Mechanochemical synthesis offers a scalable route to engineer defect-rich structures and cation disorder, as demonstrated in $Li_2ZrCl_6$ systems.[15] Post-synthesis annealing of zirconium-based halide, however, often sacrifices these beneficial non-periodic features, highlighting a trade-off between crystallinity and ionic mobility.[15,16]

In this work, we introduce $Nb^{5+}$ into the $Li_2ZrCl_6$ lattice to synthesize $Li_{2-x}Zr_{1-x}Nb_xCl_6$ ($0 \le x < 1$) halide SSEs via aliovalent substitution. This strategy leverages the close ionic radius of $Nb^{5+}$ to $Zr^{4+}$ ($rNb^{5+}$ = 0.68 Å vs. $rZr^{4+}$ = 0.72 Å) to minimize phase transition while inducing lithium vacancies and optimizing $Li^+$ migration pathways. Through mechanical ball milling, we achieve enhanced ionic conductivity and reduced activation energy. Structural analyses and density functional theory (DFT)-based climbing-image nudged elastic band (CI-NEB) calculations reveal the effects of $Nb^{5+}$ substitution on the local lattice environment and $Li^+$ transport properties, and establish a paradigm for designing high-performance halide SSEs.

The structural integrity and compositional homogeneity of $Li_{2-x}Zr_{1-x}Nb_xCl_6$ ($0 \le x < 1$) were systematically characterized using X-ray diffraction (XRD) and scanning electron microscopy (SEM). As shown in Figure 1a. the XRD patterns confirm that the pristine $Li_2ZrCl_6$ (LZC) crystallizes in the trigonal system with the space group $P\bar{3}m1$, consistent with prior studies.[15] Notably, the incorporation of $Nb^{5+}$ into the LZC lattice does not induce any new Bragg peaks, indicating the formation of a solid solution without phase transitions. This can be attributed to the close ionic radii of $Nb^{5+}$ (0.68 Å) and $Zr^{4+}$ (0.72 Å), which minimize phase transition while enabling successful substitution. The selection of doping elements is critical, as significant differences in ionic radii can lead to structural degradation. For instance, substitution of $Yb^{3+}$ in $Li_3YbCl_6$ with $Zr^{4+}$ induces a trigonal-to-orthorhombic phase transition due to the large radius difference between $Zr^{4+}$ (0.72 Å) and $Yb^{3+}$ (0.86 Å).[17] In contrast,

[a] College of Chemistry and Chemical Engineering, Central South University, Changsha 410083, China.
[b] Hunan Provincial Key Laboratory of Chemical Power Sources, Changsha 410083, China.
† These authors contributed equally to this work.

View Article Online
DOI: 10.1039/D5CC02055H

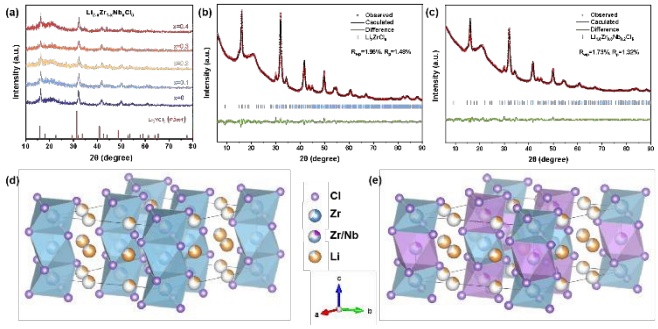


**Figure 1.** (a) XRD patterns of $Li_{2-x}Zr_{1-x}Nb_xCl_6$ (0≤x<1) synthesized via mechanical ball milling. (b, c) Rietveld refinements of room-temperature XRD data for LZC and LZNC. (d, e) Crystal structures of LZC and LZNC.

the close radii of $Nb^{5+}$ and $Zr^{4+}$ prevent such phase transitions, aligning with findings in $Li_{3-x}In_{1-x}Hf_xCl_6$.[18]

Rietveld refinement of the XRD data (Figures 1b and 1c) confirms that the crystal structure retains the P$\bar{3}$m1 space group with no significant changes in lattice parameters. The crystal structures of LZC and LZNC are depicted in Figures 1d and 1e. Specifically, a trigonal lattice is formed by the arrangement of Li and Zr octahedra, with the LiCl6 octahedra connected via edge or face sharing (Figure S1). Detailed structural parameters for LZC are provided in Table S1. Li occupies two different Wyckoff sites (6g and 6h), while Cl occupies the 6i Wyckoff sites. The cell parameters of LZNC are listed in Table S2, showing that Nb atoms occupy the 1b and 2d Wyckoff sites alongside Zr atoms. With increasing $Nb^{5+}$ content, the lattice parameters of LZNC decrease to a = 10.9410(55) Å, c = 5.9268(60) Å, resulting in a reduced cell volume. This contraction is attributed to the smaller ionic radius of $Nb^{5+}$ compared to $Zr^{4+}$.

The surface morphology of LZC and LZNC was analyzed using SEM (Figures S2 and S3). Both materials exhibit uniform nanoscale particle distributions. Energy-dispersive spectroscopy (EDS) mapping confirms the homogeneous distribution of Zr, Nb, and Cl elements in LZNC. These results validate the successful substitution of $Nb^{5+}$ into the LZC lattice and highlight the structural stability of the synthesized halide solid-state electrolytes (SSEs).

Electrochemical impedance spectroscopy (EIS) was employed to evaluate the ionic conductivity of $Li_{2-x}Zr_{1-x}Nb_xCl_6$ (0≤x<1). The Nyquist plots and corresponding room-temperature ionic conductivities (25 ℃) are shown in Figure 2a and 2b. Notably, the optimal composition $Li_{1.8}Zr_{0.8}Nb_{0.2}Cl_6$ (LZNC) exhibits a room-temperature ionic conductivity of $1.03\times10^{-3}$ S $cm^{-1}$, doubling that of pristine $Li_2ZrCl_6$ (LZC). This improvement is attributed to the generation of lithium vacancies and the optimization of $Li^+$ migration pathways induced by $Nb^{5+}$ substitution. By measuring Nyquist plots for $Li_{2-x}Zr_{1-x}Nb_xCl_6$ (0≤x<1) at various temperatures (Figure 2c and S4), the ionic conductivities were found to follow the Arrhenius relationship (Figure 2d). The calculated activation energies are inverse to the room-temperature ionic conductivities (Figure 2e). At x=0.2, LZNC achieves a minimum activation energy of 0.327 eV, corresponding to the peak of the volcano-shape ionic conductivity curve. This behavior aligns with previously reports on aliovalent substitution in halide SSEs.[10] The decrease in ionic conductivity for x>0.2 is attributed to the excess $Nb^{5+}$ substitution, which causes vacancy oversaturation and excessive lattice contraction, thereby hindering $Li^+$ migration . Thus, precise control of $Nb^{5+}$ substitution is critical to achieving optimal ionic conductivity.

Additionally, low electronic conductivity is essential for effective electrolytes to prevent charge leakage. Shown in Figure S5 are DC polarization curves for LZC and LZNC under different voltages, from which the electronic conductivities are obtained to be $8.11\times10^{-9}$ S $cm^{-1}$ and $1.09\times10^{-9}$ S $cm^{-1}$ for LZC and LZNC, respectively (Figure 2f). Compared to the ionic conductivity of LZNC, the electronic conductivity is six orders of magnitude lower. This high ionic conductivity combined with ultra-low electronic conductivity enables LZNC a highly competitive SSE for ASSLIBs.

Density functional theory (DFT)-based climbing-image nudged elastic band (CI-NEB) calculations were conducted to investigate the $Li^+$ transport mechanisms. Figure S6 illustrates the migration trajectories of lithium ions within $ZrCl_6$ and $(Zr/Nb)Cl_6$ octahedra. The movement of $Li^+$ between the Li 6h and 6g Wyckoff sites along the c-axis forms a complete transport channel parallel to the c-axis. Notably, after Nb doping, $Li^+$ diffusion is significantly enhanced in the a-b plane perpendicular to the c-axis, in addition to the initial c-direction pathway. Each Li2 atom is connected to other Li2 atoms along the a or b direction, forming a 3D $Li^+$ percolating network in LZNC, which facilitates efficient $Li^+$ transport.

By calculating energy barriers for all transport paths marked in Figures 3a, 3b and S7, the [Li1-Li2-Li1] chain parallel to the c-axis (i.e., the [001] direction) was identified as the most utilized migration pathway due to its lowest energy barrier compared to other transport chains. Additionally, the [Li1-i1-Li1-i2-i2-Li1] and [Li2-i3-Li2] chains within the a-b plane are also effective pathways for $Li^+$ transport. The vacancies between the purple spheres do not indicate an inability of Li ions to migrate but rather represent regions of relatively low $Li^+$ density. Comparing the migration pathway energy barriers of LZC and LZNC (Figure 3c, d), the latter shows a significant reduction in

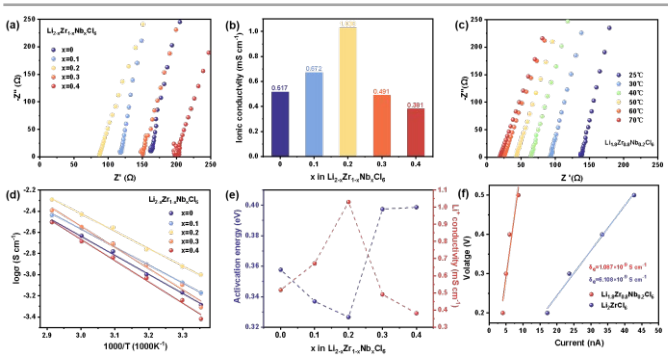


**Figure 2.** (a) Nyquist plots and (b) ionic conductivities of $Li_{2-x}Zr_{1-x}Nb_xCl_6$ (0≤x<1) at room temperature. (c) Nyquist plots of LZNC at different temperatures. (d) Arrhenius relationship plots and (e) activation energies alongside room-temperature ionic conductivities of $Li_{2-x}Zr_{1-x}Nb_xCl_6$ (0≤x<1). (f) Electronic conductivities of LZC and LZNC at 25 ℃.

migration barriers across nearly all directions. Notably, the energy barrier of the [Li2-i3-Li2] chain decreases by 15% after Nb doping, resulting in an effective barrier of only 0.562 eV. This reduction is attributed to the enhanced connectivity of Li2 atoms in the a-b plane, consistent with the simulated motion trajectories in Figure 3b. It is noted that the CI-NEB method simulates ion transport in an idealized state. Actual transport is influenced by non-periodic features such as local defects and amorphous phases introduced by high-speed mechanical ball milling. Consequently, the theoretical migration barrier does not perfectly match the experimentally determined activation energy (0.327 eV). The non-periodic features introduced by mechanical ball milling are favourable for reducing migration barriers. Determining the exact nature of these features remains challenging with current characterization techniques and represents an important direction for future research.

The enhanced ionic conductivity of $Li_{2-x}Zr_{1-x}Nb_xCl_6$ ($0 \le x < 1$) can be attributed to the beneficial effects of high-valent $Nb^{5+}$. Firstly, the introduction of $Nb^{5+}$ increases the concentration of lithium vacancies due to charge compensation. Secondly, comparing Figures 1b and 1c reveals that the diffraction peak intensity of LZNC is reduced relative to LZC. This indicates that high-energy ball milling introduces abundant non-periodic features and reduces crystallinity. The combination of increased lithium vacancy concentration and the presence of non-periodic structures significantly contributes to the improved lithium-ion conductivity. However, excessive vacancies can encroach on $Li^+$ sites, reducing carrier concentration and limiting further conductivity improvements. Figure S8 shows that annealed-LZNC exhibits an ionic conductivity of only $1.46\times10^{-7}$ S $cm^{-1}$ at room temperature after annealing at 250°C for 5 hours, a significant decrease compared to unannealed LZNC. This is attributed to the destruction of non-periodic features such as site disorder during the sintering process.[19,20] Importantly, $Nb^{5+}$ substitution also optimizes $Li^+$ transport paths in the a-b plane at the microscopic level, enhancing $Li^+$ transport efficiency and thereby increasing ionic conductivity.

The electrochemical stability of LZC and LZNC was evaluated using linear sweep voltammetry (LSV). As shown in Figure S9, the onset potential of the anodic current for LZNC is 4.02 V (vs. Li/$Li^+$), slightly higher than that of LZC. This implies that LZNC is compatible with 4V-class cathode materials for ASSLIB applications. However, chloride-based electrolytes face a common challenge: their non-zero reduction potentials make them susceptible to non-self-limited reactions with Li metal, due to the coexistence of ionic and electronic conductor reduction products.[21,22] Consequently, most chloride electrolytes cannot directly contact Li metal.[23]

The superior mechanical ductility of halide SSEs allows cathode composites to be prepared by manual milling with cathode active materials, forming an effective ionic/electronic percolation network (Figure 4a).[19] The SEM image and EDS mapping of the prepared composite cathode material show a uniform distribution of Cl around Co, confirming the tight wrapping combination of the two (Figure 4b). The surface morphology and elemental distribution of the cold-pressed composite cathode sheets reveal a uniform encapsulation of the cathode active material by halide SSEs (Figure S10). This is critical for achieving efficient ion/electron mixing. To prevent reactions between the anode and electrolyte, a layer of LPSC was inserted between them to suppress side reactions. The structure of the resulting ASSLIB and corresponding elements distribution are shown in Figure 4c and Figure S11, with the electrolyte layer in direct contact with the cathode.

The electrochemical performance of LZC and LZNC -based ASSLIBs was tested at 0.2 C (1C = 140 mAh $g^{-1}$) within a voltage window of 2.5~4.2V, respectively. Figure 4d shows the initial charge/discharge voltage curves of the two cells. The LZC-based cell achieved an initial Coulombic efficiency of 92.35% and a discharge capacity of 118.16 mAh $g^{-1}$. In contrast, the LZNC-based cell exhibited a higher initial Coulombic efficiency of 95.19% and a first discharge specific capacity of 127.4 mAh $g^{-1}$. The rate capability of the LZC and LZNC cells is shown in Figure 4e. When the rate increases from 0.2 C to 0.4 C, the capacity of

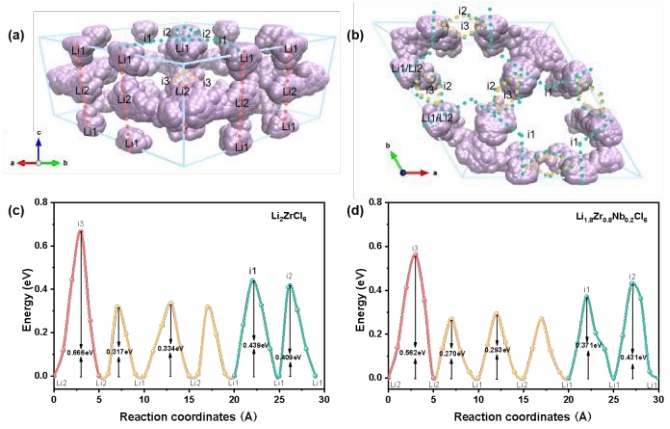


**Figure 3.** (a, b) $Li^+$ migration pathways and (c,d) corresponding energy barriers in LZC and LZNC.

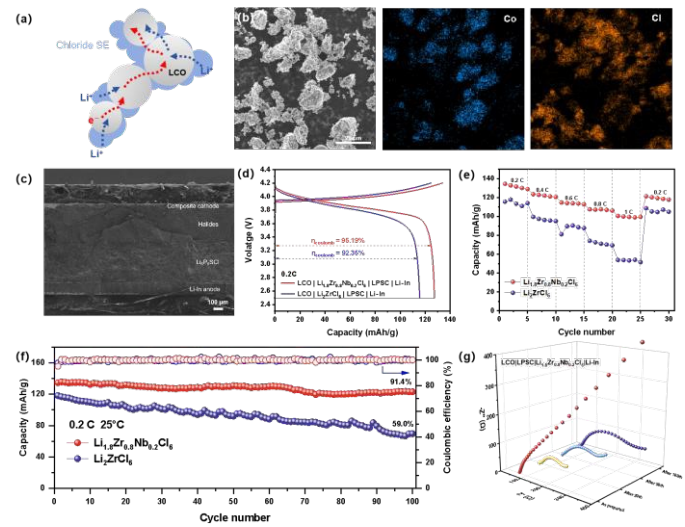


**Figure 4.** (a) Schematic diagram of the mixed ionic/electronic network, and (b) SEM and corresponding EDS mapping of Co and Cl elements for the LCO composite cathode. (c) Cross-sectional SEM, (d) initial charge/discharge curves at 0.2 C, (e) rate capability at 0.2, 0.4, 0.6, 0.8, and 1 C, (f) long-term cycling performance at 0.2 C, and (g) Nyquist plots before and after 20, 50, and 100 cycles at 0.2 C for assembled ASSLIBs.

View Article Online
DOI: 10.1039/D5CC02859K





the LZNC cell decreases only slightly, while the LZC cell experiences significant capacity fading. The LZNC battery maintains average capacities of 122.1, 113.9, and 107.1 mAh $g^{-1}$ at 0.4 C, 0.6 C, and 0.8 C, respectively, and still retains 100 mAh $g^{-1}$ at 1 C, significantly outperforming the LZC cell (50 mAh $g^{-1}$ at 1 C). Notably, when the current density back to 0.2 C, the reversible capacity of the LZNC cell recovers to 92% of its initial capacity. Long-term cycling stability was also evaluated. As shown in Figure 4f, after 100 cycles, the LZNC battery retains 91.4% of its discharge capacity with a Coulombic efficiency exceeding 99.8%, while the LZC cell retains only 59% of its capacity. Enhanced cycling stability is due to the tightly stabilized composite cathode and improved transport efficiency from $Nb^{5+}$ doping, highlighting the significance of ionic conductivity in improving ASSLIBs performance.

To evaluate the interfacial stability of LZC and LZNC ASSLIBs, we observed the changes in electrochemical impedance spectra (EIS) with increasing number of cycles. It was found that the interfacial impedances for both batteries were slowly increased as the semicircles were growing gradually (Figure 4g and Figure S12). But the LZNC battery presented significantly smaller impedance values than the LZC, indicative of a better interfacial charge-transfer capability by rational $Nb^{5+}$ doping.

In summary, we successfully developed a series of $Nb^{5+}$-substituted $Li_{2-x}Zr_{1-x}Nb_xCl_6$ halide solid-state electrolytes through aliovalent doping and mechanical ball milling. The substitution of $Zr^{4+}$ with $Nb^{5+}$ significantly enhances ionic conductivity by introducing lithium vacancies, optimizing lattice parameters, and constructing 3D $Li^+$ transport networks. The optimal $Li_{1.8}Zr_{0.8}Nb_{0.2}Cl_6$ exhibits a room-temperature ionic conductivity of $1.03 \times 10^{-3}$ S $cm^{-1}$ and a low activation energy of 0.327 eV, outperforming pristine $Li_2ZrCl_6$. DFT-based CI-NEB calculations confirm large reduced $Li^+$ migration barriers in c-axis directions, enabling rapid ion diffusion. ASSLIBs incorporating this electrolyte demonstrate excellent electrochemical performance, including high-rate capability (100 mAh $g^{-1}$ at 1 C) and long-term cyclability (91.4% capacity retention after 100 cycles). These findings underscore the effectiveness of aliovalent substitution in tailoring inorganic halide SSEs and pave the way for their application in safe, high-energy-density ASSLIBs. Future work should focus on improving interfacial stability with lithium metal anodes and scaling up synthesis processes for industrial adoption.

This work was financially supported by the National Natural Science Foundation of China (52174284, 22478444), the Key Research and Development Program of Hunan Province (2024JK2094), the Hunan Provincial Natural Science Foundation of China (2023JJ40707), and the Hunan Provincial Science and Technology Plan Projects of China (2017TP1001). We are grateful to the High-Performance Computing Center of Central South University for assistance with the computations.

## Conflicts of interest

There are no conflicts to declare.

## Data Availability

The data supporting this article have been included as part of the Supplementary Information.

## Notes and references

1 A. Manthiram, X. Yu and S. Wang, *Nat. Rev. Mater.*, 2017, **2**, 16103.
2 W. D. Richards, L. J. Miara, Y. Wang, J. C. Kim and G. Ceder, *Chem. Mater.*, 2016, **28**, 266–273.
3 Z. Yang, H. Yuan, C. Zhou, Y. Wu, W. Tang, S. Sang and H. Liu, *Chem. Eng. J.*, 2020, **392**, 123650.
4 T. Famprikis, P. Canepa, J. A. Dawson, M. S. Islam and C. Masquelier, *Nat. Mater.*, 2019, **18**, 1278–1291.
5 C. Wang, J. Liang, J. T. Kim and X. Sun, *Sci. Adv.*, 2022, **8**, eadc9516.
6 T. Asano, A. Sakai, S. Ouchi, M. Sakaida, A. Miyazaki and S. Hasegawa, *Adv. Mater.*, 2018, **30**, 1803075.
7 X. Li, J. Liang, J. Luo, M. Norouzi Banis, C. Wang, W. Li, S. Deng, C. Yu, F. Zhao, Y. Hu, T.-K. Sham, L. Zhang, S. Zhao, S. Lu, H. Huang, R. Li, K. R. Adair and X. Sun, *Energy Environ. Sci.*, 2019, **12**, 2665–2671.
8 Z. Li, Y. Mu, K. Lü, G. Kang, T. Yang, S. Huang, M. Wei, L. Zeng and Y. Li, *Angew. Chem. - Int. Ed.*, 2025, **64**, e202501749.
9 X. Li, J. Liang, K. R. Adair, J. Li, W. Li, F. Zhao, Y. Hu, T.-K. Sham, L. Zhang, S. Zhao, S. Lu, H. Huang, R. Li, N. Chen and X. Sun, *Nano Lett.*, 2020, **20**, 4384–4392.
10 T. P. Poudel, E. Truong, I. P. Oyekunle, M. J. Deck, B. Ogbolu, Y. Chen, P. K. Ojha, T. N. D. D. Gamaralalage, S. V. Patel, Y. Jin, D. Hou, C. Huang, T. Li, Y. Liu, H. Xiong and Y.-Y. Hu, *ACS Energy Lett.*, 2025, **10**, 40–47.
11 S. Y. Kim, K. Kaup, K.-H. Park, A. Assoud, L. Zhou, J. Liu, X. Wu and L. F. Nazar, *ACS Materials Lett.*, 2021, **3**, 930–938.
12 L. Shen, J. Li, W. Kong, C. Bi, P. Xu, X. Huang, W. Huang, F. Fu, Y. Le, C. Zhao, H. Yuan, J. Huang and Q. Zhang, *Adv. Funct. Mater.*, 2024, **34**, 2408571.
13 Y. Ye, Z. Gu, J. Geng, K. Niu, P. Yu, Y. Zhou, J. Lin, H. J. Woo, Y. Zhu and J. Wan, *Nano Lett.*, 2025, **25**, 3747–3755.
14 Q. Wang, Y. Zhou, X. Wang, H. Guo, S. Gong, Z. Yao, F. Wu, J. Wang, S. Ganapathy, X. Bai, B. Li, C. Zhao, J. Janek and M. Wagemaker, *Nat. Commun.*, 2024, **15**, 1050.
15 K. Wang, Q. Ren, Z. Gu, C. Duan, J. Wang, F. Zhu, Y. Fu, J. Hao, J. Zhu, L. He, C.-W. Wang, Y. Lu, J. Ma and C. Ma, *Nat Commun*, 2021, **12**, 4410.
16 S. Zhang, F. Zhao, L.-Y. Chang, Y.-C. Chuang, Z. Zhang, Y. Zhu, X. Hao, J. Fu, J. Chen, J. Luo, M. Li, Y. Gao, Y. Huang, T.-K. Sham, M. D. Gu, Y. Zhang, G. King and X. Sun, *J. Am. Chem. Soc.*, 2024, **146**, 2977–2985.
17 J. Liang, X. Li, K. R. Adair and X. Sun, *Acc. Chem. Res.*, 2021, **54**, 1023–1033.
18 K. Tuo, C. Sun, C. A. López, M. T. Fernández-Díaz and J. A. Alonso, *J. Mater. Chem. A*, 2023, **11**, 15651–15662.
19 K. Tuo, C. Sun and S. Liu, *Electrochem. Energy Rev.*, 2023, **6**, 17.
20 R. Schlem, S. Muy, N. Prinz, A. Banik, Y. Shao-Horn, M. Zobel and W. G. Zeier, Adv. Energy Mater., 2020, **10**, 1903719.
21 Y. Fu and C. Ma, *Sci. China Mater.*, 2021, **64**, 1378–1385.
22 L. M. Riegger, R. Schlem, J. Sann, W. G. Zeier and J. Janek, *Angew Chem Int Ed*, 2021, **60**, 6718–6723.
23 X. Li, J. Liang, X. Yang, K. R. Adair, C. Wang, F. Zhao and X. Sun, *Energy Environ. Sci.*, 2020, **13**, 1429–1461.

View Article Online
DOI: 10.1039/D5CC02859K

## Data availability statements

The data supporting this article have been included as part of the Supplementary Information.